Geomorphology 433 (2023) 108727

Contents lists available at ScienceDirect

Geomorphology

journal homepage: www.journals.elsevier.com/geomorphology

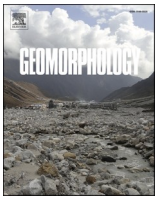

Monitoring solifluction movement in space and time: A semi-automated high-resolution approach

M.R. Harkema [a], W. Nijland [a], S.M. de Jong [a], T. Kattenborn [b,c], J. Eichel [a,*]

[a] Utrecht University, Physical Geography, Princetonlaan 8A, 3584 CB Utrecht, the Netherlands
[b] Leipzig University, Remote Sensing Centre for Earth System Research, Talstrasse 35, 04103 Leipzig, Germany
[c] German Centre for Integrative Biodiversity Research (iDiv), Puschstrasse 4, 04103 Halle-Jena-Leipzig, Germany

ARTICLE INFO

Keywords:
Solifluction lobes
Mass Movement
Co-alignment
COSI-Corr
Feature-Tracking
UAV

ABSTRACT

Solifluction is the slow downslope movement of soil mass due to freeze-thaw processes. It is widespread on hillslopes in Polar and Alpine regions and contributes substantially to sediment transport. As solifluction lobe movement is in the order of millimeters to centimeters per year, it is difficult to measure with high spatial and temporal resolution and accuracy. In this study we developed a semi-automated approach to monitor movement using unmanned aerial vehicles, image co-alignment, and COSI-Corr (Co-registration of Optically Sensed Images and Correlation) to track slope movement from orthophotos. The method was applied on yearly images acquired between 2017 and 2021 of three solifluction lobes with different degrees of vegetation cover along an elevational gradient in Turtmann Valley, Swiss Alps. We found movement patterns across all three lobes with highest movement rates at the solifluction lobes center and lowest rates at lobe fronts. Overall, at the highest elevations (2560 m) lobe movement rates were highest with up to 14.0 cm yr^{-1} and intermediate elevations (2417 m) had the lowest values up to 2.9 cm yr^{-1}. The lobe at the lowest elevation (2170 m) showed intermediate movement rates with up to 4.9 cm yr^{-1} for single years. Our monitoring approach provides yearly, spatially extensive movement estimates across the complete spatial extent of a lobe for each 1 cm^2 of its surface, strongly increasing measurement resolution in comparison to traditional solifluction monitoring approaches using point measurements. In comparison to previous close-range remote sensing approaches, the use of a co-alignment procedure for the acquired drone data enabled a time-saving field setup without Ground Control Points (GCPs). The resulting high co-registration accuracy enabled us to detect solifluction movement if it exceeds 5 mm with sparse vegetation cover. Dense vegetation cover limited feature-tracking but detected movement rates and patterns are in the same order of magnitude and matched previous measurements using classical total station measurements at the lowest, mostly vegetated lobe. This study demonstrates the use of drone-based Digital Elevation Models (DEMs) and orthophotos in a semi-automated method which reaches the high spatiotemporal resolution necessary to detect subtle movements of solifluction lobes at yearly intervals at the sub-centimeter scale. This provides new insights into solifluction movement and how much it contributes to sediment transport. Therefore, our semi-automated approach has a great potential to uncover the fundamental processes and better understand solifluction movement.

1. Introduction

Solifluction is the slow downslope movement of soil mass due to freeze-thaw processes occurring on hillslopes in Polar and Alpine regions usually in the order of millimeters to centimeters per year (French, 2007; Matsuoka, 2001). Despite these low rates, solifluction contributes substantially to sediment transport and total slope retreat due to its widespread spatial distribution (Berthling et al., 2002; Draebing and Eichel, 2018; Matsuoka, 2001). Therefore, it is essential to understand the solifluction processes that occur in these areas and the landforms they create. Solifluction is classified into four processes: frost creep, needle ice creep, gelifluction and plug-like flow (Matsuoka, 2001). These processes can continuously rework slope material without creating distinct landforms or shape the slope material in the form of solifluction sheets, solifluction terraces or solifluction lobes (Ballantyne, 2018; Glade et al., 2021; Van Everdingen, 2005). There are several types

* Corresponding author.
E-mail address: j.eichel@uu.nl (J. Eichel).

https://doi.org/10.1016/j.geomorph.2023.108727
Received 20 July 2022; Received in revised form 13 April 2023; Accepted 5 May 2023
Available online 11 May 2023

of tongue-shaped solifluction lobes consisting of lobe tread and riser, with turf-banked solifluction lobes (TBLs) characterized by fronts covered by vegetation (Benedict, 1970). Commonly TBLs have a steep (15°–60°) fronts called the lobe riser and a relatively smooth upper surface called the lobe tread (Van Everdingen, 2005). A TBL develops when the rates of soil movement decrease downslope, strong vertical frost sorting is absent and the sediment flow is channelized (Benedict, 1976). Glade et al. (2021) recently suggested that solifluction lobes are comparable to fluid-like instabilities, arising due to the competition of gravity and cohesion. Recent research also suggested a role of vegetation for TBL development (Eichel et al., 2020, 2017), which provides cohesion at the lobe risers. The solifluction processes that work on a TBL are mainly annual frost creep and/or gelifluction, inducing deep (30 to 60 cm) and slow movement of the soil (Matsuoka, 2001). This effect is created by the presence of vegetation since vegetation on a TBL prevents diurnal frost creep and needle ice creep. Other factors controlling the development and movement include material properties (e.g., Harris et al., 2008; Matsuoka, 2001), topographic controls (Draebing and Eichel, 2017), climatic controls (e.g. Glade et al., 2021) and the occurrence of permafrost (Eichel et al., 2020; Matsuoka and Hirakawa, 2000).

Measuring TBL movement can be difficult since the movement is very slow and not continuous, mostly happening during initial winter freezing and spring snow melt (Jaesche et al., 2003). TBLs move in the range of millimeter to centimeter per year (Benedict, 1970; Eichel et al., 2020). The highest amount of movement is found at the lobe tread, with the lowest movement values at the lobe risers (Benedict, 1970; Eichel et al., 2020; Gengnian et al., 1995; Klingbeil et al., 2019). The TBL movement is mostly lower than the resolution of traditional or remote techniques. Traditionally, solifluction movement is measured by using tape or point geodetic measurements of markers at the surface (e.g., Kellerer-Pirklbauer, 2018; Kinnard and Lewkowicz, 2005; Matsuoka, 2010; Ridefelt et al., 2011). Below the surface, strain probes, potentiometers or inclinometers are installed at several depths to assess the amount of movement of the TBL (Jaesche et al., 2003; Kinnard and Lewkowicz, 2005; Matsuoka, 2010). Recently, remote sensing approaches have been developed, using Satellite Synthetic Aperture Radar Interferometry (InSAR) to assess solifluction movement at landscape scale (Rouyet et al., 2021, 2019). Other methods tested on solifluction lobes are Terrestrial Laser Scanner (TLS) point clouds (Holst et al., 2021; Klingbeil et al., 2019) or manual feature-tracking on orthophotos created with Unmanned Aerial Vehicles (UAVs; Eichel et al., 2020) However, to reach the needed measurement accuracy, these approaches are still time consuming. For indirect georeferencing using local coordinate systems, stable points need to be set up in the field (Eichel et al., 2020; Holst et al., 2021). However, this is problematic as stable ground control points are very rare on solifluction slopes, and increases fieldwork, data processing and analysis time, e.g., for point cloud or image co-registration. In addition, differential GPS precision is usually bigger (>1–2 cm) than solifluction movement rates in mountain areas, rendering direct georeferencing difficult to impossible (Holst et al., 2021; Klingbeil et al., 2019) because true movement cannot be separated from measurement errors. Therefore, a fast, (semi-) automatic method to map TBL movement with a high spatiotemporal resolution at a landform scale is currently missing. This method would make it possible to monitor larger numbers of solifluction lobes across the landscape, increasing understanding of solifluction movement and its controls. This understanding is strongly needed to understand past, current, and future climate change impacts on periglacial landscapes and their connected ecosystems.

To develop a (semi-) automated method for high spatiotemporal resolution TBL movement monitoring at a landform scale, the combination of two existing methods appears promising. The first method is the use of automatic co-alignment of images collected with UAVs, also called united bundle adjustment or time-SIFT (Cook and Dietze, 2019; Feurer and Vinatier, 2018; Li et al., 2017). The overlapping collected aerial images of one survey are combined in a 3D space to create a point cloud, Digital Elevation Model (DEM) and orthophoto in a process called photogrammetry (Anders et al., 2019). With co-alignment, the collected images from multiple surveys are processed together, which enables the generation of spatially co-registered point clouds, DEMs or orthophotos with pixel sizes in the order of centimeters (Anders et al., 2019; Cook and Dietze, 2019; de Haas et al., 2021; Nota et al., 2022). In comparison, older methods used to align different sets of images by relying on Ground Control Points (GCPs) or Global Positioning System (GPS), sometimes in combination with Real Time Kinematic (RTK) (Lucieer et al., 2014). Images that do not have GCPs or RTK signals can be included and the same precision of the relative co-registration can be achieved (de Haas et al., 2021; Nota et al., 2022). Therefore, co-alignment is a very promising method to apply to the movement of solifluction lobes. In previous research, co-aligned orthophotos have been used for manual change detection (de Haas et al., 2021; Nota et al., 2022). (Semi-) Automated techniques for feature-tracking, to create spatially continuous movement tracking, can also be applied to the co-alignment products. One of the (semi-) automated feature-tracking techniques is COSI-Corr: Co-registration of Optically Sensed Images and Correlation (Ayoub et al., 2017). COSI-Corr is a software developed to accurately orthorectify, co-register and correlate images with the goal of retrieving ground deformation between before and after images (Ayoub et al., 2017; Lucieer et al., 2014). It has been used in multiple disciplines, to measure co-seismic deformation (Chen et al., 2020), glacier flow (Herman et al., 2015; Kraaijenbrink et al., 2016), rock glacier movement (Heid and Kääb, 2012), sand dune migration (Michel et al., 2018), slow landslides (Lucieer et al., 2014) and other applications in which co-registration of images is needed. This makes COSI-Corr a suitable technique to use for (semi-) automated tracking of TBL movement.

The aim of this study was to develop a semi-automated approach to map the movement of solifluction lobes with a high spatiotemporal resolution. The objectives are to:

1. Demonstrate the efficacy of UAV image co-alignment on TBLs.
2. Apply COSI-Corr on UAV image time series of solifluction lobes and evaluate ground movement detection performance.
3. To compare and evaluate the movement of three turf-banked solifluction lobes on an elevation gradient.

2. Methods

2.1. Study area

The three TBLs (Table 1) that are the focus of this paper are located along an elevational gradient in the Turtmann Valley, Valais, Switzerland (Fig. 1B). This is a north-south oriented tributary of the Rhône valley (Eichel et al., 2013), dominated by the Turtmann and neighboring Brunegg glaciers that are at the south end of the valley (Draebing and Eichel, 2018). The valley is a Pleistocene glacial trough with fifteen hanging valleys on both sides of the upper valley slopes (Eichel et al., 2013). The most southern hanging valley on the east side of the Turtmann Valley is the Pipjitälli (Fig. 1A), which contains two of the three lobes examined in this paper. The Pipjitälli has an elevation

Table 1
The three TBLs and their properties from field observations of Eichel et al. (2017, 2020).

Properties	Lobi	Lobert	Lobidita
Elevation (m a.s.l.)	2170–2185	2417–2427	2560–2567
Riser height (m)	1.8	0.95	0.6
Length (m)	29	18	12
Width (m)	14	12	12
Aspect	North	West	West
Slope (°)	22	32	22
Parent slope (°)	23	33	33

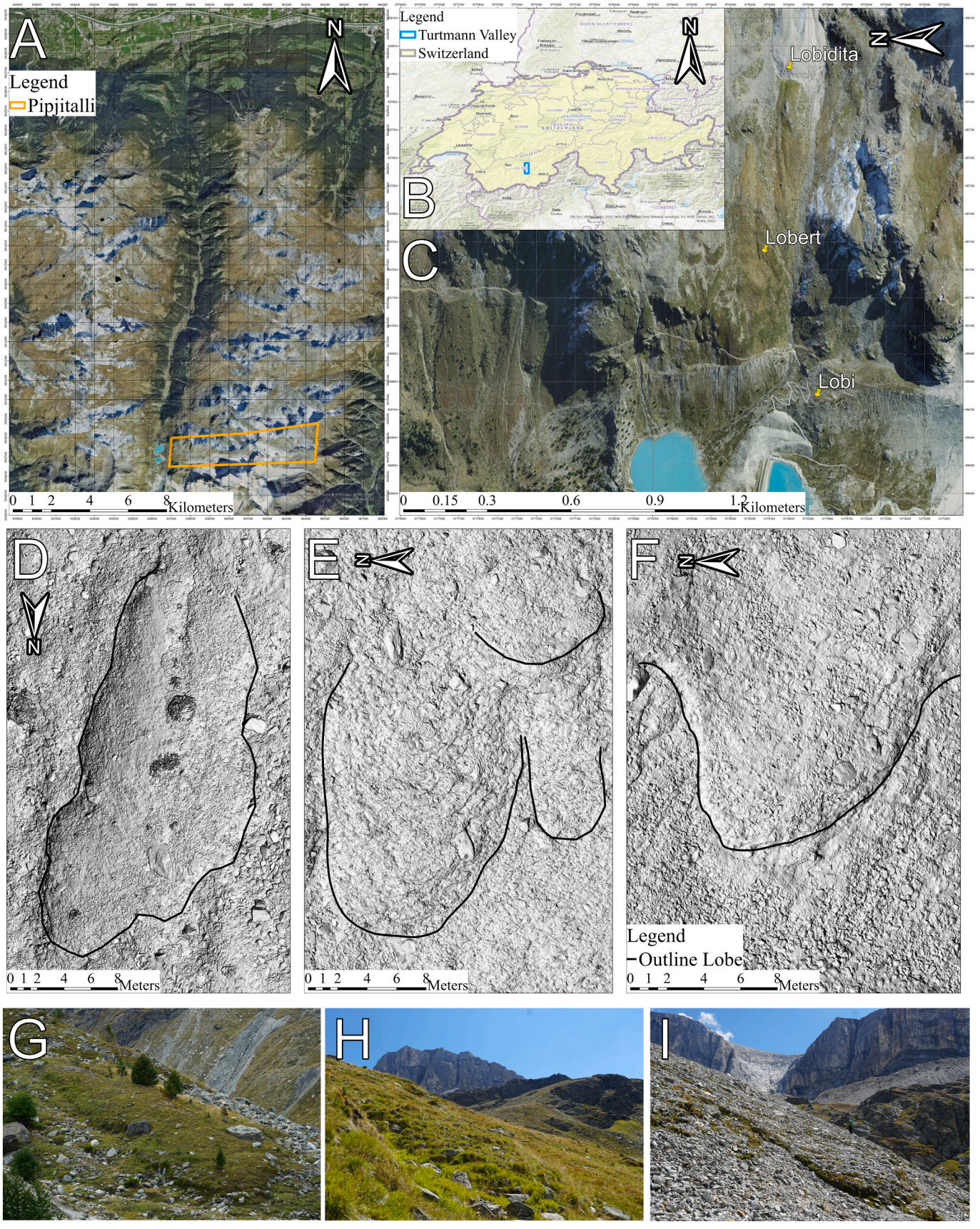

Fig. 1. Location of the Pipjitälli (A) in the Turtmann Valley (B) and the TBLs (C) in Switzerland, with the three researched TBLs Lobi (D, G), Lobert (E, H) and Lobidita (F, I) shown on hillshaded DEMs (D, E, F) and on fieldwork photos (G, H, I).

between 2456 m and 2922 m above sea level (a.s.l.), and contains active, inactive and relict rock glaciers, solifluction lobes, moraine deposits, talus and block slopes and a small glacier (Otto et al., 2009). The nearest weather station is located in the glacier foreland of the Turtmann Valley at 2180 m a.s.l. and has recorded mean annual air temperatures of 1.8 to 3.89 °C and annual precipitation from 720.4 to 835.4 mm between 2014 and 2017 (MeteoSwiss, 2017). All three TBLs are below the lower limit of permafrost, which therefore, is not considered to influence the current solifluction movement (Eichel et al., 2020; Kenner et al., 2019).

The TBL with the lowest elevation, here called "Lobi", is located on a lateral moraine created by a small advance of the Turtmann glacier in 1925 (Eichel et al., 2020; Table 1; Fig. 1D, G). Lobi's vegetation covers a very large part of the TBL and consists of herbs, shrubs, and a few small trees. The TBL at middle elevation, "Lobert", is located in the hanging valley Pipjitälli (Table 1; Fig. 1E, H). Lobert has the highest vegetation cover of the three TBLs, consisting of herbs and shrubs. The TBL at the highest elevation of the three, "Lobidita", is located in the Pipjitälli on top of a relict rock glacier (Otto et al., 2009; Rasemann, 2004; Table 1; Fig. 1F, I). The vegetation on Lobidita consists of several small patches on the lobe tread, with the largest vegetation patches present on the lobe riser.

2.2. UAV surveys

UAV surveys were carried out at the end of August from 2017 to 2021 for each of the three TBLs during fieldwork in the Turtmann Valley. The survey characteristics are shown in Table 2. The surveys from 2017, 2018 and 2019 were carried out with the Phantom 4 Pro Plus drone, and the surveys from 2020 and 2021 were carried out with the Phantom 4 RTK drone. GCPs were placed on and besides the lobes to support visual interpretation of the co-alignment and feature-tracking results. In 2017 the drone was flown manually, the surveys carried out in 2018, 2019, 2020 and 2021 were all flown twice, with a manual and an automatic, pre-programmed flight. The flight height of the manual flight was ~15 m, and the automatic flight was ~20 m for the Phantom 4 Pro Plus drone and ~25 m for the Phantom 4 RTK drone. All images have a sampling distance of millimeters to centimeters, depending on the local topography and flight height. The automatic flights from 2020 and 2021 were not used in the co-alignment process, because a large difference in flight altitude with the other datasets prevented successful co-alignment.

2.3. Co-alignment

We processed the drone imagery in Agisoft Metashape Professional (Version 1.7.3) using SfM multi-survey co-alignment (Cook and Dietze, 2019; de Haas et al., 2021; Nota et al., 2022). The photographs of all multidate surveys per lobe are aligned together (Appendix A), using the default settings of 40,000 key points and 4000 tie points limits without 'reference preselection', resulting in a shared set of tie points for the block adjustment procedure. We improved alignment accuracy by removing tie points with a reconstruction uncertainty larger than 50, a projection accuracy larger than 10, and a reprojection error larger than 0.5 for Lobert and larger than 1.0 for Lobi and Lobidita. After these steps, the alignment was optimized using adaptive camera model fitting. After the co-alignment procedure the image set was split into the separate years and without changing image geometry. A dense point cloud was generated for each year with a high quality and mild depth filtering. The dense point cloud was optimized by filtering by confidence, where the points with a confidence of 1 were removed. From the dense point clouds, a DEM was created for each year. The dense point clouds were interpolated using default settings for the resolution and pixel size, with a geographic projection and interpolation enabled. The DEM was used to rectify the images and create an orthophoto by projecting the individual aerial images on the DEM. For this, the settings for mosaic blending mode and hole filling were enabled. The resulting DEMs and orthophotos had resolutions between 0.31 cm/pixel and 1.13 cm/pixel. Therefore, to facilitate optimal comparison of the images acquired in the different years, all DEMs were interpolated with a resolution of 1 cm/pixel and the orthophotos with a resolution of 0.5 cm/pixel.

Table 2
UAV survey timing, number of images and acquisition altitude.

	Lobi	Lobert	Lobidita
Image acquisition (date)			
2017	17 August	17 August	17 August
2018	21 August	22 August	22 August
2019	23 August	25 August	25 August
2020	25 August	27 August	27 August
2021	23 August	24 August	24 August
Total number of images	2453	1934	3391
Average flying altitude (m)	15.9	15.8	20.4

2.4. COSI-Corr for feature-tracking

To semi-automatically determine the movement of the three TBLs between the different years, we used COSI-Corr. COSI-Corr is a software module integrated into the ENVI image analysis software. It can correlate optical remotely sensed images such as UAV images with the objective of retrieving ground surface deformation from multi-temporal images (Ayoub et al., 2017). COSI-Corr works on single-band greyscale images. To determine the band that gives the best result, we used the frequency correlator with default settings on the available red, green and blue bands. The signal-to-noise ratio layer (SNR) calculated from the green band has the highest mean and lowest standard deviation, which indicates that the green band has the highest measured quality of the three bands and is therefore the best choice (Yang et al., 2020). We used the frequency correlation algorithm to correlate the orthophotos of different years, since the available data from the TBLs is relatively noise-free (Ayoub et al., 2017). The frequency correlator requires several initial values: (1) the initial and final window size; (2) the step size; (3) the robustness iteration; and (4) the mask threshold (Ayoub et al., 2017; Chen et al., 2020; Das, 2021; Leprince et al., 2012). For the robustness iteration and the mask threshold we used values that are used almost consistently throughout the literature and give good results (Chen et al., 2020; Das, 2021; Hassan et al., 2021; Yang et al., 2020; Zhang et al., 2021; Appendix B). We determined the correct step size by running the frequency correlator with a step size of 1, 4, 8 and 16 pixels. There were no notable differences between the results. Therefore, we chose the smallest possible value of a step size of one pixel. To determine the correct initial and final window sizes, we used a combination of the methods used by Lucieer et al. (2014) and Yang et al. (2020). Yang et al. (2020) calculated 15 different possibilities of initial and final window sizes, from which the window sizes that had a smoothing effect or a salt-and-pepper effect could be eliminated. By using the visual interpretation approach from Lucieer et al. (2014) the best window size for this paper was determined at 64 pixels as an initial size and 32 pixels as a final size. This also corroborates with the rule of thumb of using window sizes at least two times the expected displacement (Ayoub et al., 2017; Das, 2021), which is for our TBLs expected to be up to 8 cm yr^{-1}. The frequency correlator produces an output map with three layers: one East-West displacement layer (EWD), one North-South displacement layer (NSD) and the signal-to-noise ratio layer (Zhang et al., 2021). East and North are the positive directions in the displacement layers and the signal-to-noise ratio helps to assess the quality of correlation between the images (Ayoub et al., 2017; Das, 2021). The EWD and NSD can be combined in vectors accurately indicating the direction of the movement (Ayoub et al., 2017; Das, 2021). To determine the displacement magnitude from the EWD and NSD layers created with COSI-Corr, we used the Euclidean distance (Das, 2021; Lucieer et al., 2014; Zhang et al., 2021):

$$\text{Displacement} = \sqrt{\text{EWD}^2 + \text{NSD}^2} \quad (1)$$

This gives the displacement as a raster map. Vegetation present on the TBLs Lobi and Lobert created high levels of noise in the displacement maps, due to its growth between the different years. In addition, leaves and small twigs likely changed position slightly during and between surveys due to wind. Therefore, we applied a mask for the vegetation, which makes the displacement of the TBL itself more visible. The threshold value for creating the mask was determined by retrieving the highest displacement value from the non-vegetated areas for all the different years. Mask threshold displacement values ranged between 0.03 and 0.05 m yr^{-1} for Lobi and between 0.03 and 0.065 m yr^{-1} for Lobert, with the highest values of 0.12 m and 0.065 m for the whole period (Appendix C).

To show the displacement as vectors on the map, a magnitude and angle needed to be calculated. The magnitude is the previously calculated displacement. We calculated the angle in degrees with the following equation:

$$\text{Angle} = \text{Atan2}\left(\frac{\text{EWD}}{\text{NSD}}\right) \times \left(\frac{180^{\circ}}{\pi}\right) \quad (2)$$

From the angle and the displacement, a magnitude-direction map is compiled, which shows the vectors of the displacement. We performed these calculations for the movement between single years and for the movement over the whole period, between 2017 and 2021. Only the displacement map from Lobidita was not determined in this way, but by adding the movement of the single years together. This was necessary because the overall displacement of Lobidita between 2017 and 2021 was too large for the current COSI-Corr settings to detect and adapting the current settings resulted in a smoothing or a salt-and-pepper effect.

To compare movement of the different solifluction lobe parts in time, we retrieved mean movement rates (Appendix D). To validate the threshold value above which the movement of the TBLs is assumed to be significant, the displacement on stable areas outside the TBLs was measured. We expect that the movement rates in these areas are equal to or less than 0.5 cm yr^{-1}. If this is correct and also corresponds with values lower than the reprojection errors of the co-alignment, the movement is assumed to be significant. However, as the areas on the edges of the orthophotos are more vulnerable for geometric inaccuracies, they are less reliable but still a useful indicator of precision.

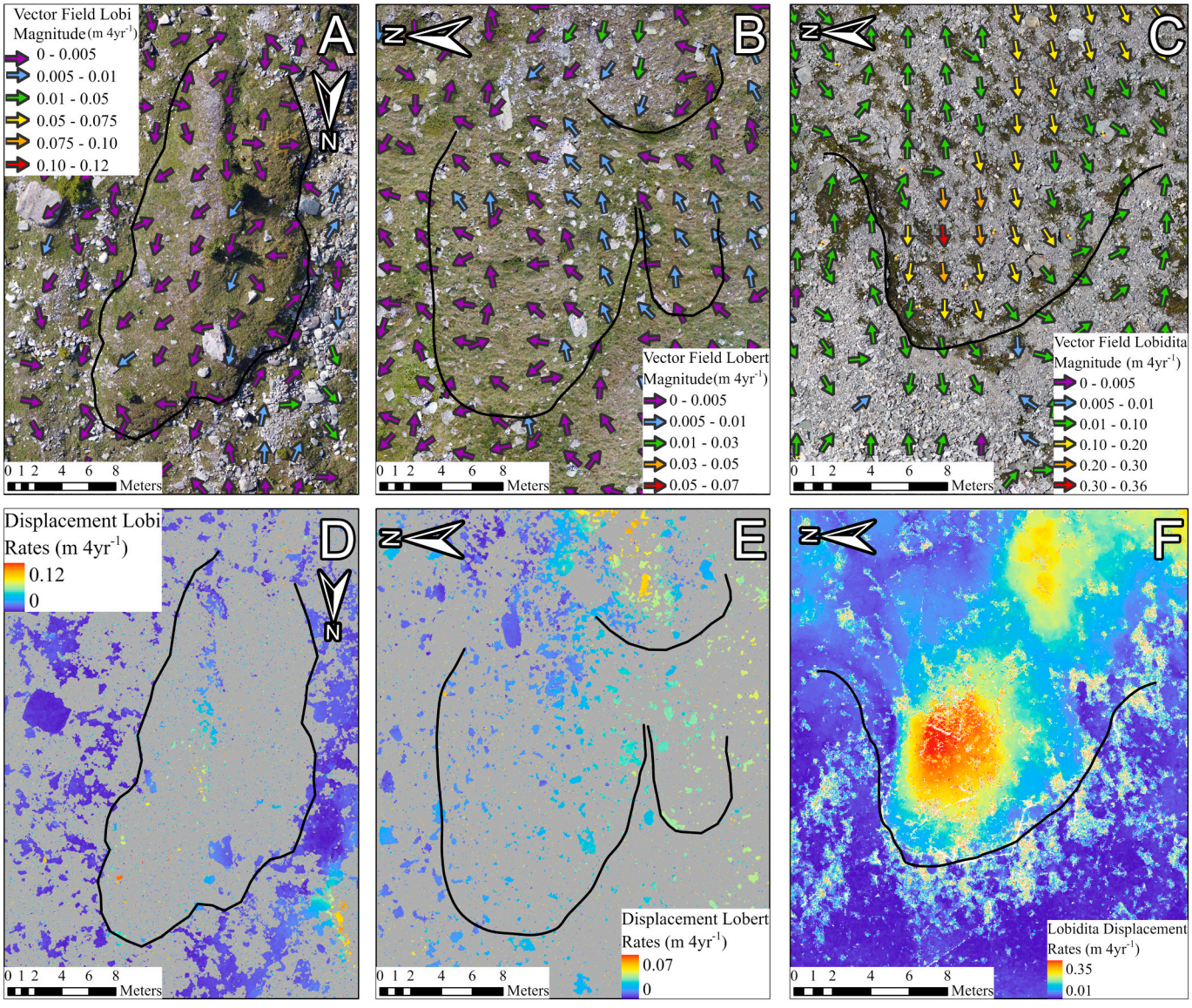

Fig. 2. Movement rates of Lobi, Lobert and Lobidita shown as vector maps (A–C) and displacement maps (D–F) between 2017 and 2021 in meter.

3. Results

3.1. Co-alignment

The co-alignment of the UAV surveys for the three TBLs resulted in orthophotos with high resolutions of 0.5 cm/pixel. Results are so accurate that additional solifluction lobes, not noticed before, became visible. For example, in Fig. 1E a second TBL is visible on the right side of Lobert, and a third TBL is visible in the top right corner. These additional lobes also show in the feature-tracking results presented later. The reprojection error of the co-alignment is 0.503 pixels for Lobi, 0.526 pixels for Lobert and 0.625 pixels for Lobidita.

3.2. Feature-tracking

With reprojection errors for all three lobes between 0.503 and 0.625 pixels, movement is assumed to be significant from 1 pixel and higher. Since the resolution of all the orthophotos is 0.5 cm/pixel, the movement was assumed to be significant for 0.5 cm and higher. This corresponds with the validation of the threshold values, since the stable areas outside the lobes all have movement rates equal to or less than 0.5 cm yr^{-1} (Figs. 2, 3).

3.3. Movement

The surface movement of Lobi between 2017 and 2021 ranges from 0 to 12.0 cm in four years (i.e., 0–3.0 cm yr^{-1}; Fig. 2A, D). The highest displacement rates generally occur on the middle and lower lobe tread with rates of 11.7 cm in four years (2.925 cm yr^{-1}). The lowest displacement rates occur on the risers and the upper lobe tread with rates of 1.8 cm in four years (0.45 cm yr^{-1}). The surface movement of Lobert between 2017 and 2021 ranges from 0 to 7.0 cm in four years (0–1.75 cm yr^{-1}; Fig. 2B, E). The highest displacement rates occur on the right side of the TBL with rates of 3.0 cm in four years (0.75 cm yr^{-1}). Higher values are visible for a second and third TBL present (Fig. 2B, E). The second TBL on the right side of Lobert has a displacement rate of 4.1 cm in four years (1.025 cm yr^{-1}) and the third TBL on the top right of the figure has a displacement rate of 6.3 cm in four years (1.575 cm yr^{-1}). The lowest displacement rates are very close to the threshold value of 0.5 cm yr^{-1} and occur on the risers and the upper lobe tread of Lobert with rates of 0.6 cm in four years (0.15 cm yr^{-1}). The surface movement of Lobidita between 2017 and 2021 ranges between 0 and 37.0 cm in four years (0–9.25 cm yr^{-1}; Fig. 2C, F). The parent slope on the north-, south- and westward side of the TBL is moving slower than the TBL itself at rates between 0 and 0.5 cm yr^{-1}. The highest displacement rates occur

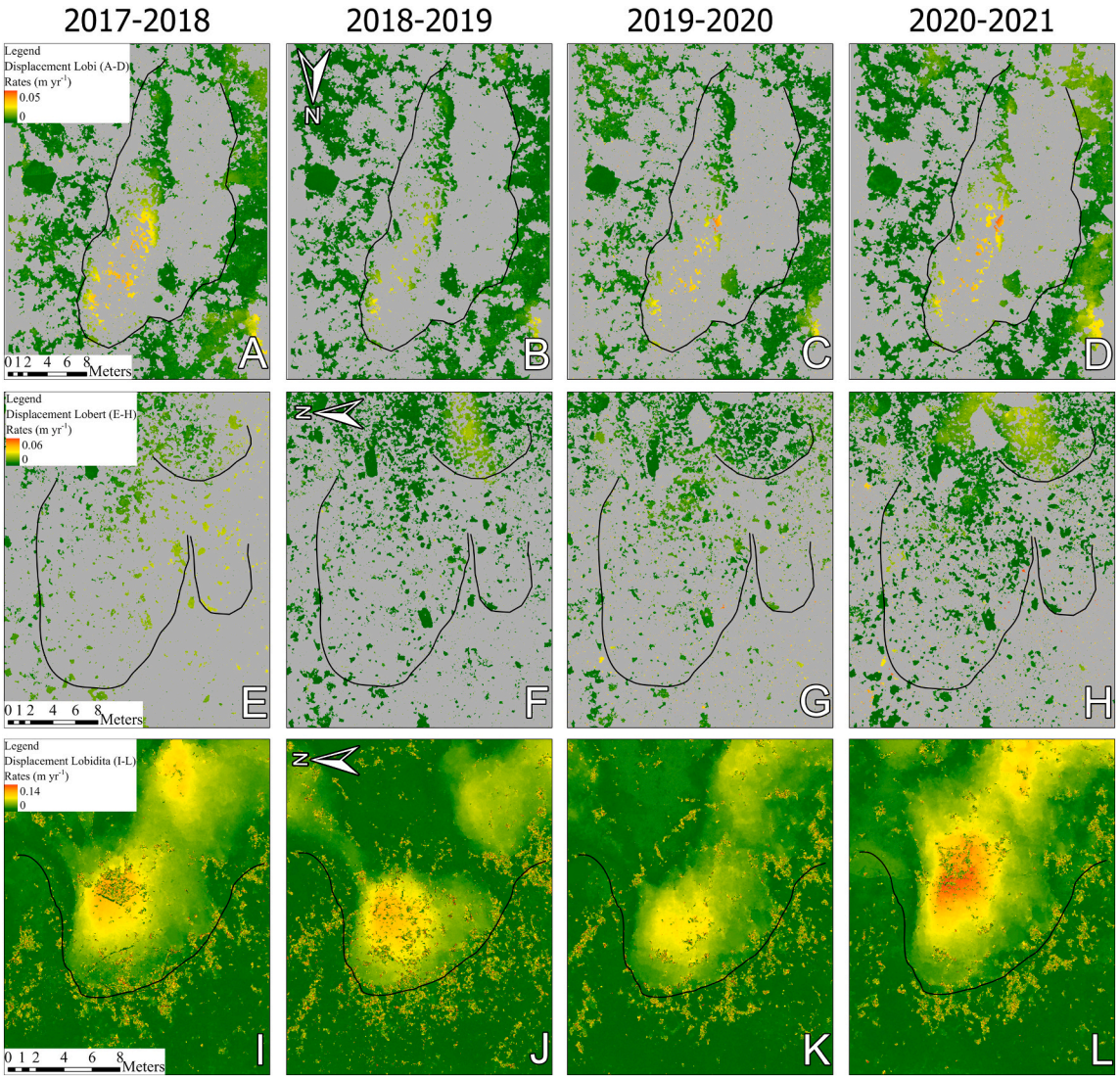

Fig. 3. Movement rates of Lobi (A–D), Lobert (E–H) and Lobidita (I–L) shown as displacement maps between 2017 and 2021 in m yr^{-1}, with the areas masked out shown in grey.

on the middle and upper lobe tread with rates of 36.1 cm in four years (9.025 cm yr^{-1}). The lowest displacement rates occur on the TBL riser with rates of 1.8 cm in four years (0.45 cm yr^{-1}). The areas considered stable outside the TBLs show movement rates between 0 and 0.5 cm in four years and can be considered as intrinsic uncertainty, which supports the assumption that lobe movement is significant above 0.5 cm yr^{-1}.

The movement rates between the single years showed nearly the same pattern as the movement over the whole period for all three lobes (Fig. 3). However, the highest movement rates differed in location and magnitude between the different years. For Lobi, the highest amount of movement of 2017–2018 and 2018–2019 is present on the lower lobe tread, while the movement of 2019–2020 and 2020–2021 is the highest in the middle of the lobe tread (Fig. 3A–D). For Lobert, the movement of 2017–2018 is high for all three visible TBLs, while the movement of 2019–2020 is low for all three TBLs and the movement of 2018–2019 and 2020–2021 is highest for the TBL in the top right corner (Fig. 3E–H). For Lobidita, the highest movement rates are between 2020 and 2021, which are also the most upslope displacements. The other years have movement more central on the TBL, with lower rates. 2019–2020 is showing the least amount of movement out of all the time steps (Fig. 3I–L). The maximum movement rates differ in location and magnitude between the different years for all three TBLs and between the three lobes.

The mean movement rates also differ in location and magnitude between the different years for all three TBLs (Fig. 4). For Lobi and Lobidita the highest mean movement rates occurred at the lobe front and lobe tread, while the lowest mean movement rates characterize the riser and the parent slope (Fig. 4A, C). The only exception for this is 2018–2019 from Lobi, where the lobe tread has the least amount of mean movement. For Lobert the highest mean movement rates occurred at the lobe tread and the lowest mean movement rates at the lobe front, with both the parent slope and the riser showing intermediate movement rates (Fig. 4C).

Comparing the three TBLs, it is clear that Lobi and Lobidita move faster than their surrounding parent slopes and that the movement patterns are very different in magnitude (Fig. 4). Lobi and Lobert have the same range of movement, while Lobidita moves much faster.

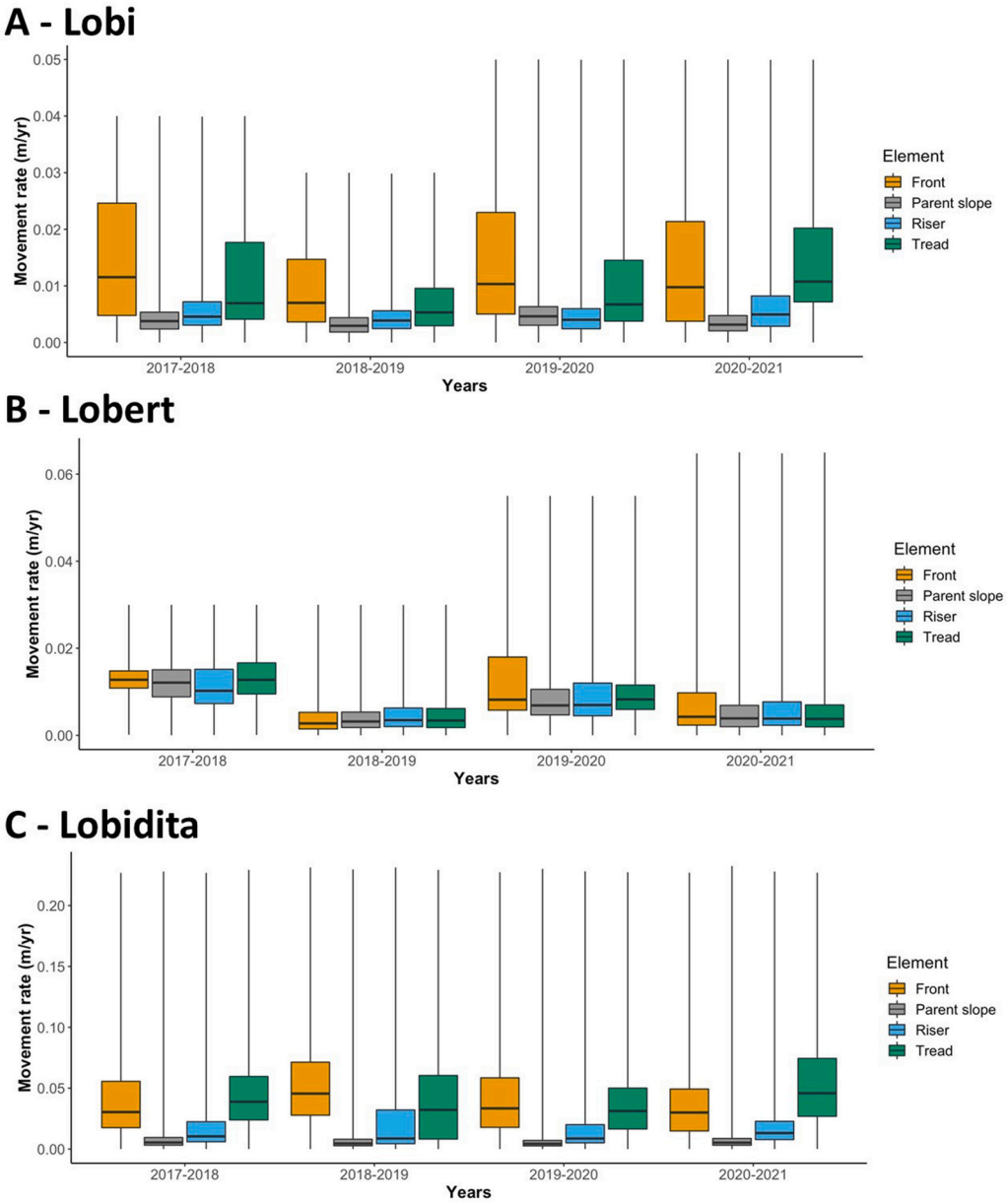

Fig. 4. Boxplot of the movement rates of the different lobe elements for Lobi (A), Lobert (B) and Lobidita (C) for the four periods between 2017 and 2021 in m yr^{-1}.

Another striking observation is that in contrast to Lobi, most of the vectors of Lobert show that the movement is upslope instead of downslope. This pattern is visible over the whole period (Fig. 2) but applies as well for the single years. However, the TBL visible in the top right of Fig. 2B next to Lobert shows downslope movement for the whole period, which applies as well for the single years.

4. Discussion

4.1. Co-alignment

Using a co-alignment workflow to create co-registered orthophotos to map the movement of TBLs resulted in very accurately co-aligned high-quality orthophotos with a very high spatial resolution of 0.5 cm/pixel. This showed that image co-alignment (Cook and Dietze, 2019), united bundle adjustment (Li et al., 2017) or time-SIFT (e.g., Feurer and Vinatier, 2018) works very well for creating co-aligned orthophotos from different years with a very high resolution for comparatively small areas. Low reprojection errors of 0.503, 0.526 and 0.625 pixels confirm this, also matching the low reprojection errors found by De Haas et al. (2021). Using co-alignment enabled us to reach accuracies below mean lobe movement rates and differential GPS precision, making it possible to detect solifluction movement in the range of mm. Using two types of drones resulted in accuracy differences for the georeferencing of the images. The Phantom 4 RTK drone equipped with network RTK corrections resulted in a spatial accuracy of millimeter to centimeter, while the Phantom 4 Pro Plus drone had an image reference accuracy of decimeters. To ensure successful alignment, the function "reference preselection" had to be turned off during the co-alignment. This resulted in the surveys collected with the Phantom 4 Plus Pro drone also being georeferenced in an accuracy of millimeter to centimeter, resulting in an overall higher accuracy. This is confirmed by Nota et al. (2022), who determined that the use of at least one RTK survey in a co-alignment workflow improves the accuracy of the surveys without RTK up to the accuracy of an RTK survey. This method is thus a good way to integrate older data, even when RTK signal and GCPs were not used in older surveys.

4.2. Feature-tracking

The use of COSI-Corr for feature-tracking resulted in highly accurate displacement maps. The COSI-Corr results yielded reliable displacement values corresponding with lobe displacement values reported by others (Benedict, 1970; Gengnian et al., 1995; Kellerer-Pirklbauer, 2018; Kinnard and Lewkowicz, 2005; Matsuoka, 2010; Table 3). One problem with the use of COSI-Corr was that seamlines resulting from mosaicking individual images into the orthophoto were visible in the displacement maps, but not in the orthophotos. There is an alternative blending method available that averages all available pixels, but this results in a visually displeasing orthomosaic, with pronounced softness which is unsuited for feature tracking. Therefore, more research is needed to develop a method to remove the seamlines in the future.

The vegetation present on the lobes presented some difficulties for the use of COSI-Corr. Vegetation changed a lot annually by growing or by slightly changing position during and between surveys due to wind. COSI-Corr detected all these vegetation changes and presented them as displacements. In previous research COSI-Corr was used on areas with minimal or no vegetation (Das, 2021; Kraaijenbrink et al., 2016; Michel et al., 2018), or on areas with a very large scale, which minimized the effect of the vegetation (Chen et al., 2020). Vegetation differences can, just as differences in illumination conditions, obstruct the COSI-Corr algorithm for identifying matching features between images collected at different dates (Lucieer et al., 2014). Therefore, COSI-Corr works best for lobes with minimal vegetation, such as Lobidita. However, we successfully managed to remove displacement caused by vegetation changes with our threshold masks created for the lobes Lobi and Lobert. Thereby, the displacement of the lobe itself became much clearer and interpretable. Despite this fact, the movement values of Lobert are just slightly above the threshold value of significant movement. This is possibly a limitation of using our method in dense vegetation and more research is needed. However, the movement values of Lobi are also slightly above the threshold value of significant movement. These values do corroborate with the movement values found through manual feature-tracking and total station measurements by Eichel et al. (2020). Therefore, our method works very well when there is no vegetation or minimal vegetation present on the lobe. Manual feature-tracking has the same problems with densely vegetated lobes, which result in a limited point density, as shown by Eichel et al. (2020). Other studies have also shown that the presence of vegetation complicates surface deformation mapping and results in a decrease in performance of image cross-correlation (Eltner et al., 2022; Peppa et al., 2017).

COSI-Corr is very sensitive to the input parameters. For most of these, the same values were used unanimously throughout literature and gave good results, but for the parameter window size different values were used (Chen et al., 2020; Das, 2021; Hassan et al., 2021; Kraaijenbrink et al., 2016; Yang et al., 2020; Zhang et al., 2021). These authors did not specify how they determined the correct window size for their research area and images used. Yet, the window size has a large impact on the final result of COSI-Corr, since small windows have large uncertainties and large windows can have a smoothing effect (Yang et al.,

Table 3
The three TBLs and their properties compared with similar areas with solifluction lobe movement from literature.

Properties	Lobi, this study	Lobert, this study	Lobidita, this study	Kellerer-Pirklbauer (2018)	Benedict (1970)	Gengnian et al. (1995)
Movement rates (cm yr^{-1})	0.2–4.4	0.1–2.7	0.2–13.6	3.5–6.8	0.3–4.3	2.1–18.77
Elevation (m a.s.l.)	2170–2185	2417–2427	2560–2567	2107–2595	3480–3640	3300–3600
Study area	Turtmann Valley, Switzerland	Turtmann Valley, Switzerland	Turtmann Valley, Switzerland	Fallbichl, Elisabethfelsen, Seeschartl, Hinteres Langtal cirque, Austria	Niwot Range, Colorado, USA	Laerdun Pass, head area of Urumqi River and Wangfeng Platform, Tianshan Mountains, China
Mean annual air temperature (MAAT)	2–4 °C	2–4 °C	2–4 °C	–	−3.3 °C	−0.3 °C
Precipitation (mm yr^{-1})	720–835	720–835	720–835	–	–	400
Aspect	North	West	West	Northeast–Northwest	Northeast–Southwest	North
Parent slope type	Lateral moraine	–	Rock Glacier	–	–	–
Movement method	COSI-Corr	COSI-Corr	COSI-Corr	Near-surface markers	Steel rods and wooden spikes	Dip-angle method
Spatiotemporal resolution	5 mm	5 mm	5 mm	One point measurement	24 point measurement	One point measurement

2020). It was therefore difficult to select the best method for determining the optimal window size for this study. Ultimately, a combination of the approaches from Yang et al. (2020) and Lucieer et al. (2014) was used. This consisted of first calculating 15 different possibilities of initial and final window sizes, from which the window sizes with a smoothening effect or a salt-and-pepper effect were eliminated. From the resulting window sizes, the best option was determined by using visual interpretation. Future studies using COSI-Corr should consider methods to determine optimal window sizes because the chosen window sizes have a considerable impact on the performance of the displacement assessment. COSI-Corr works well with the input orthophotos, which are mosaics of images from the surface. As a consequence, the resulting displacement rates are valid only for the surface and do not provide information about subsurface movements or deformations. Previous research by Price (1970), Matsuoka (2001) and Kellerer-Pirklbauer (2018), among others, shows that the movements at the surface are often stronger than subsurface movements. For future solifluction research, a promising approach would be to combine our semi-automated method to detect surface movement with classical methods to detect subsurface solifluction movement, such as strain probes, near-surface markers or potentiometers (Jaesche et al., 2003; Kellerer-Pirklbauer, 2018; Matsuoka, 2010). In comparison to other recent studies using remote sensing methods to investigate movement of individual solifluction lobes (Eichel et al., 2020; Holst et al., 2021; Klingbeil et al., 2019), our semi-automatic approach combining co-alignment with COSI-Corr feature-tracking can save considerable time both in field as well as in later processing and data analysis.

4.3. Solifluction movement in space and time

The displacement and vector movement maps (Figs. 2, 3), are spatially continuous and have a much finer spatial resolution than previously available for solifluction lobes, with a few exceptions (Holst et al., 2021). Up to now, for many lobes only point measurements were available on the lobe tread or risers for one year or several years at one depth or along a depth profile (Benedict, 1970; Eichel et al., 2020; Gengnian et al., 1995; Jaesche et al., 2003; Kellerer-Pirklbauer, 2018). The increase in spatial and temporal resolution of our approach strongly improves the understanding of the movement behavior of single and multiple TBLs. All three lobes have the highest movement rates at the tread and lowest movement rates at the lobe risers (Fig. 2). This corresponds with observations reported by, for example Benedict (1970) and Gengnian et al. (1995). Eichel et al. (2020) found similar movement patterns for Lobi using total station measurements. Our study also shows that patterns differ between individual lobes and for individual lobes in time. Rouyet et al. (2021) recently found that solifluction movement increases with slope gradient across a mountain landscape, with highest movement above 30° slope gradient. However, this does not match with our slope scale results as Lobi with a slope gradient of 23° is moving faster than Lobert at slope gradient 33°. Previous studies furthermore found that the middle of the lobe moves fastest (e.g., Benedict, 1970; Gengnian et al., 1995), which matches with the lobes Lobi and Lobidita, but not with Lobert. Lobert further has the strongest movements occurring where least vegetation is present. This is caused by either the movement being easiest trackable in these areas or by the movement being strongest in these areas as no stabilizing vegetation is present (Eichel et al., 2017). For Lobi, the temporal movement analysis (Figs. 3A–D, 4A) shows that the maximum amount of movement has different values throughout the years, with the highest movement in 2020–2021 and the lowest movement in 2018–2019. This is also the case for Lobert and partially for Lobidita (Fig. 3E–H, I–L). Lobidita also had the highest movement in 2020–2021, but the least amount of movement in 2019–2020. This could be explained by differences in thermal, hydrological and snow melt conditions and timing between the years (Jaesche et al., 2003), but this needs more research for confirmation. Furthermore, the locations where the highest movement is present changes between the subsequent years for Lobi and Lobidita. For Lobi it changes from the lower lobe tread in 2017–2018 with 0.037 m yr^{-1} and 2018–2019 with 0.025 m yr^{-1} to the upper lobe tread in 2019–2021 with 0.048 m yr^{-1}, while for Lobidita the highest movement changes from the upper lobe tread in 2017–2018 with 0.10 m yr^{-1} to the lower lobe tread in 2018–2019 with 0.10 m yr^{-1} and 2019–2020 with 0.07 m yr^{-1} and back to the upper lobe tread in 2020–2021 with 0.14 m yr^{-1} (Figs. 3A–D, I–L, 4A, C; Appendix D). The mean movement rates of the different lobe parts also differ between the different years for Lobi and Lobidita. For Lobi the highest mean movement rates are for the lobe front for 2017–2020 and for the lobe tread for 2020–2021 (Fig. 4A). This pattern is also visible for Lobidita, but the lobe tread also has a higher mean movement rate in 2017–2018 than the lobe front (Fig. 4C). These high spatiotemporal differences in lobe movement have not been reported before, since most studies in literature regarding temporal movement data focused on single point movement on the lobes, and not spatially across the lobe (Benedict, 1970; Gengnian et al., 1995; Kellerer-Pirklbauer, 2018).

The amount of movement found for the TBLs Lobi, Lobert and Lobidita ranges from a maximum of 2.7 cm yr^{-1} for Lobert to a maximum of 13.6 cm yr^{-1} for Lobidita. The movement rates for Lobi and Lobert are similar to movement rates reported for similar areas. However, the movement rates of Lobidita are much higher compared to other lobes. Gengnian et al. (1995) found similar movement rates for solifluction lobes in the Tianshan Mountains, China (Table 3). The solifluction lobes in this area are located much higher, with much less precipitation per year and lower annual mean temperatures. Despite these climatic differences, the displacement rates are very similar. For the Tianshan Mountains, high movement rates have been explained by the presence of permafrost, which inhibits infiltration of moisture and allows the active layer to be easily saturated (Gengnian et al., 1995). These favorable moisture conditions promote solifluction movement. However, there is no permafrost underneath the TBLs in the Turtmann Valley, thus, other factors need to play a role for quick movement of Lobidita, such as thermal and snow conditions (Jaesche et al., 2003) or possibly the lack of vegetation (Eichel et al., 2020, 2017). The thickness of the lobes, particle sizes or the effect of the root systems of plants can possibly also have an influence on the movement behavior of the TBLs. For example, the root system of the plant species *Dryas octopetala* can increase shear strength and internal friction and thereby stabilize the slope and reduce the amount of solifluction (Draebing and Eichel, 2017; Eichel et al., 2017; Ghestem et al., 2014; Graf et al., 2009). However, more research is needed to the effect of lobe thickness, particle sizes and the influence of vegetation on TBL movement.

Another striking observation is that, while movement rates of Lobert are comparable to rates reported elsewhere, movement patterns are very irregular, there is very little difference in movement between the different lobe elements, and the vectors are directed uphill instead of downhill for almost all the calculated timesteps. Large errors in the calculations are excluded as the lobe present in the top right corner of Fig. 2B is showing downhill movement despite the high vegetation density across the lobes. One possible explanation for the behavior of the vectors is surface lowering of the tread as the lobe moves forwards and piles up at the riser (Kinnard and Lewkowicz, 2006), causing very slight tilting of the lobe tread that we detected within the COSI-Corr calculations. However, this possible explanation does not correspond to field observations in our study area, but has been found by Rouyet et al. (2021). Another explanation could be the presence of ploughing boulders which COSI-Corr tracked that could tilt as they create a furrow in the underlying soil. While the movement we detected is comparable to the speed of the ploughing boulders, with values between 3.1 and 23.2 mm yr^{-1} (Ballantyne, 2001), the orthophotos show that there are only a few boulders present on and around Lobert that could possibly be ploughing boulders (Fig. 1E). These cannot explain why almost the whole lobe moves upslope instead of downslope. The only explanation given in literature for upslope movement is retrograde frost creep, which

is the apparent upslope displacement caused by non-vertical settling during the spring and summer thaw (Benedict, 1970). This also cannot be the explanation for the upwards movement of Lobert either, since the effect of retrograde frost creep would not be visible in data collected once a year, which is the case for this study. Another explanation could be that the upslope movement of Lobert is possibly linked to the very little difference in movement between the different lobe elements of Lobert. This could result from the limited precision of the co-alignment, but as mentioned before this is very unlikely as the lobe present in the top right corner of Fig. 2B is showing downhill movement above the resolution of the images of 0.5 cm. Another explanation could be the fact that the parent slope and Lobert itself are moving only very slowly (Fig. 4B). According to literature it is assumed that lobes move quicker than their parent slopes, which are usually also affected by solifluction (Benedict, 1970; Eichel et al., 2020). For Lobert, this seems not to be true as Lobert has possibly stabilized and now moves in the same speed as its surroundings. However, to confirm this theory more research is needed. Concluding, the movement behavior of Lobert is a special case and needs further investigation.

5. Conclusions

We developed a semi-automated approach to map the movement of three turf-banked solifluction lobes at different elevations with a high spatiotemporal resolution. Our results show that:

1. Consistent movement patterns were mapped using our methods across all lobes. Lobe movement rates were highest with up to 14.0 cm yr^{-1} at the highest elevations (2560 m) and lowest with up to 2.9 cm yr^{-1}. In general, movement had the highest rates at the lobe tread and the lowest rates at the lobe risers. Our results agree in general with previously found lobe movement rates and patterns, but also demonstrate that solifluction movement magnitude and exact location are highly variable between single years and strongly differed between lobes. More research is needed to unravel the environmental controls for varying lobe movement rates and patterns in time and space.
2. A co-alignment procedure made it possible to acquire UAV data without GCPs, enabling an efficient field setup and saving subsequent data processing time. Using co-alignment, older surveys can easily be integrated and georeferenced with new high accuracy UAV data. The combination of GCP-less UAV surveys, co-alignment and semi-automated COSI-Corr feature tracking creates a highly time-efficient semi-automated workflow applicable to monitor solifluction and other slow-moving surfaces with a high temporal and very high spatial resolution.
3. The high co-registration accuracy enabled the detection of solifluction movement if it exceeds 0.5 cm with sparse vegetation. Dense vegetation cover limited feature-tracking but movement threshold masks made results for vegetation covered lobes interpretable. Detected movement rates and patterns match previous measurements using a total station at the lobe “Lobi”.

We demonstrate that the use of co-alignment and the feature-tracking algorithm COSI-Corr can create high spatiotemporal resolution image products allowing the accurate monitoring of movement rates of turf-banked solifluction lobes. This was not feasible without the accuracy and time efficiency reported here. This approach yields an even better insight into the small-scale spatiotemporal variations of TBL movement and improves the understanding of the used methods and the movement behavior of TBLs. This is important for the understanding of the geomorphological and ecological role of TBLs in a changing climate.

Declaration of competing interest

The authors declare that they have no known competing financial interests or personal relationships that could have appeared to influence the work reported in this paper.

Data availability

The data will be used for another manuscript in preparation and will be made available when the other manuscript is published.

Acknowledgements

This study was partly carried out within the BIMODAL (Biogeomorphic dynamics on lateral moraines in the Turtmann glacier foreland, Switzerland) project, funded by the German Research Foundation DFG (DI 414/22-1). Vehicle access to the Turtmann glacier foreland was kindly granted by GOUGRA AG. The authors thank Maarten J. Zeylmans van Emmichoven and Dennis Swanink for their assistance in getting COSI-Corr up and running and three anonymous reviewers whose comments greatly improved the manuscript. Fieldwork assistance by Johannes Senn, Lisa Hauer, Till Mayer, Simon Schäffler, Helle Daling Nannestad, Daniel Draebing and Constance Berends is highly appreciated.

Appendix A. Co-alignment procedure

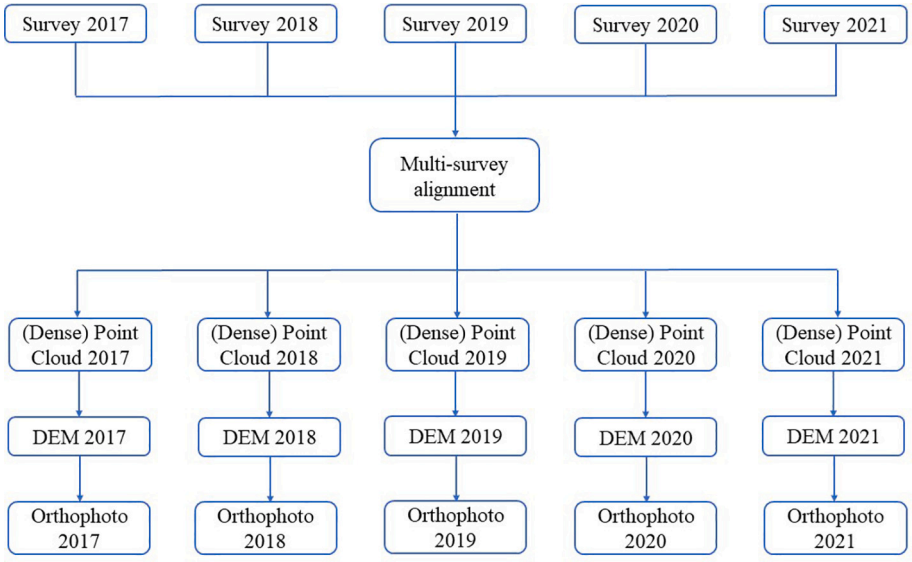

Fig. A.1. Co-alignment procedure for processing annual UAV lobe images, adapted from De Haas et al. (2021).

Appendix B. COSI-CORR settings

Table B.1
COSI-CORR settings from the frequency correlator.

Setting	Value
Used band	Green
Robustness iteration	2
Mask threshold	0.9
Step size	1
Initial window size	64 × 64
Final window size	32 × 32

Appendix C. Mask threshold displacement values

Table C.1
The mask threshold displacement values in m yr^{-1} for the single years and in m for the whole time period for the TBLs Lobi and Lobert.

Years	Lobi	Lobert
2017–2021	0.12	0.065
2017–2018	0.04	0.03
2018–2019	0.03	0.03
2019–2020	0.05	0.055
2020–2021	0.05	0.065

Appendix D. Selection of the different parts of the TBLs

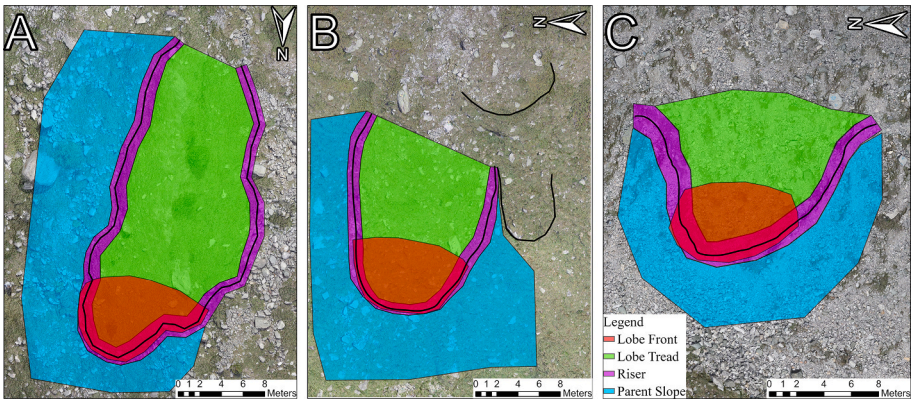

Fig. D.1. The selection of the lobe front, lobe tread, the riser and the parent slope of Lobi (A), Lobert (B) and Lobidita (C), shown on hillshaded DEMs overlain by partly transparent high resolution orthophotos taken in 2021.

References

Anders, N., Valente, J., Masselink, R., Keesstra, S., 2019. Comparing filtering techniques for removing vegetation from uav-based photogrammetric point clouds. Drones 3, 3. https://doi.org/10.3390/drones3030061.

Ayoub, F., Leprince, S., Keene, L., 2017. User's Guide to COSI-CORR Co-registration of Optically Sensed Images and Correlation. In: Calif. Inst. Technol, Pasadena, CA, USA, p. 38.

Ballantyne, C.K., 2018. Periglacial Geomorphology. Wiley-Blackwell, Hoboken, NJ.

Ballantyne, C.K., 2001. Measurement and theory of ploughing boulder movement. Permafr. Periglac. Process. 12, 267–288. https://doi.org/10.1002/ppp.389.

Benedict, J.B., 1976. Frost creep and gelifluction features: a review. Quat. Res. 6, 55–76. https://doi.org/10.1016/0033-5894(76)90040-5.

Benedict, J.B., 1970. Downslope Soil Movement in a Colorado Alpine Region: rates, Processes, and Climatic significance. Arct. Alp. Res. 2, 165–226. https://doi.org/10.1080/00040851.1970.12003576.

Berthling, I., Etzelmüller, B., Larsen, C.K., Nordahl, K., 2002. Sediment fluxes from creep processes at Jomfrunut, southern Norway. Nor. Geogr. Tidsskr. 56, 67–73. https://doi.org/10.1080/002919502760056378.

Chen, K., Avouac, J.P., Aati, S., Milliner, C., Zheng, F., Shi, C., 2020. Cascading and pulse-like ruptures during the 2019 Ridgecrest earthquakes in the Eastern California Shear Zone. Nat. Commun. 11, 3–10. https://doi.org/10.1038/s41467-019-13750-w.

Cook, K.L., Dietze, M., 2019. Short Communication: a simple workflow for robust low-cost UAV-derived change detection without ground control points. Earth Surf. Dyn. 7, 1009–1017. https://doi.org/10.5194/esurf-7-1009-2019.

Das, S., 2021. Glacier Surface Velocities in the Chandrabhaga Massif, Western Himalaya (India) Derived Using COSI-Corr From Landsat Images. https://doi.org/10.21203/rs.3.rs-598072/v1.

de Haas, T., Nijland, W., McArdell, B.W., Kalthof, M.W.M.L., 2021. Case report: optimization of topographic change detection with UAV structure-from-motion photogrammetry through survey co-alignment. Front. Remote Sens. 2, 1–9. https://doi.org/10.3389/frsen.2021.626810.

Draebing, D., Eichel, J., 2018. Divergence, convergence, and path dependency of paraglacial adjustment of alpine lateral moraine slopes. L. Degrad. Dev. 29, 1979–1990. https://doi.org/10.1002/ldr.2983.

Draebing, D., Eichel, J., 2017. Spatial Controls of Turf-Banked Solifluction Lobes and their Role for Paraglacial Adjustment in Glacier Forelands. Permafr. Periglac. Process. 28, 446–459. https://doi.org/10.1002/ppp.1930.

Eichel, J., Draebing, D., Kattenborn, T., Senn, J.A., Klingbeil, L., Wieland, M., Heinz, E., 2020. Unmanned aerial vehicle-based mapping of turf-banked solifluction lobe movement and its relation to material, geomorphometric, thermal and vegetation properties. Permafr. Periglac. Process. 31, 97–109. https://doi.org/10.1002/ppp.2036.

Eichel, J., Draebing, D., Klingbeil, L., Wieland, M., Eling, C., Schmidtlein, S., Kuhlmann, H., Dikau, R., 2017. Solifluction meets vegetation: the role of biogeomorphic feedbacks for turf-banked solifluction lobe development. Earth Surf. Process. Landforms 42, 1623–1635. https://doi.org/10.1002/esp.4102.

Eichel, J., Krautblatter, M., Schmidtlein, S., Dikau, R., 2013. Biogeomorphic interactions in the Turtmann glacier forefield, Switzerland. Geomorphology 201, 98–110. https://doi.org/10.1016/j.geomorph.2013.06.012.

Eltner, A., Hoffmeister, D., Kaiser, A., Karrasch, P., Klingbeil, L., Stöcker, C., Rovere, A., 2022. UAVs for the Environmental Sciences; Image Sequence Processing. wbg Academic.

Feurer, D., Vinatier, F., 2018. Joining multi-epoch archival aerial images in a single SfM block allows 3-D change detection with almost exclusively image information. ISPRS J. Photogramm. Remote Sens. 146, 495–506. https://doi.org/10.1016/j.isprsjprs.2018.10.016.

French, H.M., 2007. The Periglacial Environment. John Wiley & Sons.

Gengnian, L., Heigang, X., Zhijiu, C., 1995. Gelifluction in the alpine periglacial environment of the Tianshan MountainsChina. Permafr. Periglac. Process. 6, 265–271. https://doi.org/10.1002/ppp.3430060308.

Ghestem, M., Veylon, G., Bernard, A., Vanel, Q., Stokes, A., 2014. Influence of plant root system morphology and architectural traits on soil shear resistance. Plant Soil 377, 43–61. https://doi.org/10.1007/s11104-012-1572-1.

Glade, R.C., Fratkin, M.M., Pouragha, M., Seiphoori, A., Rowland, J.C., 2021. Arctic soil patterns analogous to fluid instabilities. Proc. Natl. Acad. Sci. U. S. A. 118, 1–9. https://doi.org/10.1073/PNAS.2101255118.

Graf, F., Frei, M., Böll, A., 2009. Effects of vegetation on the angle of internal friction of a moraine. For. Snow Landsc. Res. 82, 61–77.

Harris, C., Kern-Luetschg, M., Smith, F., Isaksen, K., 2008. Solifluction Processes in an Area of Seasonal Ground Freezing, DovrefjellNorway. Permafr. Periglac. Process. 19, 31–47. https://doi.org/10.1002/ppp.

Hassan, J., Chen, X., Muhammad, S., Bazai, N.A., 2021. Rock glacier inventory, permafrost probability distribution modeling and associated hazards in the Hunza River Basin, Western KarakoramPakistan. Sci. Total Environ. 782, 146833 https://doi.org/10.1016/j.scitotenv.2021.146833.

Heid, T., Kääb, A., 2012. Evaluation of existing image matching methods for deriving glacier surface displacements globally from optical satellite imagery. Remote Sens. Environ. 118, 339–355. https://doi.org/10.1016/j.rse.2011.11.024.

Herman, F., Beyssac, O., Brughelli, M., Lane, S.N., Leprince, S., Adatte, T., Lin, J.Y.Y., Avouac, J.P., Cox, S.C., 2015. Erosion by an Alpine glacier. Science (80-.) 350, 193–195. https://doi.org/10.1126/science.aab2386.

Holst, C., Janßen, J., Schmitz, B., Blome, M., Dercks, M., Schoch-Baumann, A., Blöthe, J., Schrott, L., Kuhlmann, H., Medic, T., 2021. Increasing spatio-temporal resolution for monitoring alpine solifluction using terrestrial laser scanners and 3d vector fields. Remote Sens. 13, 1192. https://doi.org/10.3390/rs13061192.

Jaesche, P., Veit, H., Huwe, B., 2003. Snow cover and soil moisture controls on solifluction in an area of seasonal frost, Eastern Alps. Permafr. Periglac. Process. 14, 399–410. https://doi.org/10.1002/ppp.471.

Kellerer-Pirklbauer, A., 2018. Solifluction rates and environmental controls at local and regional scales in Central Austria. Nor. Geogr. Tidsskr. 72, 37–56. https://doi.org/10.1080/00291951.2017.1399164.

Kenner, R., Noetzli, J., Hoelzle, M., Raetzo, H., Phillips, M., 2019. Distinguishing ice-rich and ice-poor permafrost to map ground temperatures and ground ice occurrence in the Swiss Alps. Cryosphere 13, 1925–1941. https://doi.org/10.5194/tc-13-1925-2019.

Kinnard, C., Lewkowicz, A.G., 2006. Frontal advance of turf-banked solifluction lobes, Kluane Range, Yukon Territory, Canada. Geomorphology 73, 261–276. https://doi.org/10.1016/j.geomorph.2005.06.010.

Kinnard, C., Lewkowicz, A.G., 2005. Movement, moisture and thermal conditions at a turf-banked solifluction Lobe, Kluane Range, Yukon territoryCanada. Permafr. Periglac. Process. 16, 261–275. https://doi.org/10.1002/ppp.530.

Klingbeil, L., Heinz, E., Wieland, M., Eichel, J., Laebe, T., Kuhlmann, H., 2019. In: On the UAV based Analysis of Slow Geomorphological Processes: A Case Study at a Solifluction Lobe in the Turtmann Valley. Proc. 4th Jt. Int. Symp. Deform. Monit. (JISDM), Athens, Greece, pp. 15–17.

Kraaijenbrink, P., Meijer, S.W., Shea, J.M., Pellicciotti, F., De Jong, S.M., Immerzeel, W. W., 2016. Seasonal surface velocities of a Himalayan glacier derived by automated correlation of unmanned aerial vehicle imagery. Ann. Glaciol. 57, 103–113. https://doi.org/10.3189/2016AoG71A072.

Leprince, S., Avouac, J., Ayoub, F., 2012. In: Ortho-rectification, Coregistration, and Subpixel Correlation of Optical Satellite and Aerial Images. U.S. Pat. No. 8. 121, p. 433.

Li, W., Sun, K., Li, D., Bai, T., Sui, H., 2017. A new approach to performing bundle adjustment for time series UAV images 3D building change detection. Remote Sens. 9, 1–8. https://doi.org/10.3390/rs9060625.

Lucieer, A., Jong, S.M.D., Turner, D., 2014. Mapping landslide displacements using Structure from Motion (SfM) and image correlation of multi-temporal UAV

photography. Prog. Phys. Geogr. 38, 97–116. https://doi.org/10.1177/0309133313515293.
Matsuoka, N., 2010. Solifluction and mudflow on a limestone periglacial slope in the Swiss Alps: 14 years of monitoring. Permafr. Periglac. Process. 21, 219–240. https://doi.org/10.1002/ppp.678.
Matsuoka, N., 2001. Solifluction rates, processes and landforms a global review. Earth Sci. Rev. 55, 107–134.
Matsuoka, N., Hirakawa, K., 2000. Solifluction resulting from one-sided and two-sided freezing: Field data from Svalbard. Polar Geosci 13, 187–201.
MeteoSwiss, 2017. Climate Data Station Turtmann, 2013-2017.
Michel, S., Avouac, J.P., Ayoub, F., Ewing, R.C., Vriend, N., Heggy, E., 2018. Comparing dune migration measured from remote sensing with sand flux prediction based on weather data and model, a test case in Qatar. Earth Planet. Sci. Lett. 497, 12–21. https://doi.org/10.1016/j.epsl.2018.05.037.
Nota, E.W., Nijland, W., Haas, T.De, 2022. International Journal of Applied Earth Observations and Geoinformation improving UAV-SfM time-series accuracy by co-alignment and contributions of ground control or RTK positioning. Int. J. Appl. Earth Obs. Geoinf. 109, 102772 https://doi.org/10.1016/j.jag.2022.102772.
Otto, J.C., Schrott, L., Jaboyedoff, M., Dikau, R., 2009. Quantifying sediment storage in a high alpine valley (Turtmanntal, Switzerland). Earth Surf. Process. Landforms 34, 1726–1742. https://doi.org/10.1002/esp.1856.
Peppa, M.V., Mills, J.P., Moore, P., Miller, P.E., Chambers, J.E., 2017. Brief communication: Landslide motion from cross correlation of UAV-derived morphological attributes. Nat. Hazards Earth Syst. Sci. 17, 2143–2150. https://doi.org/10.5194/nhess-17-2143-2017.
Price, L.W., 1970. Morphology and Ecology of Solifluction Lobe Development - Ruby Range. Yukon Territory. Univ, Illinois Urbana-Champaign.
Rasemann, S., 2004. Geomorphometrische Struktur eines mesoskaligen alpinen geosystems. Dr. Diss. Univ. Bonn 1–353.
Ridefelt, H., Boelhouwers, J., Etzelmüller, B., 2011. Local variations of solifluction activity and environment in the Abisko MountainsNorthern Sweden. Earth Surf. Process. Landforms 36, 2042–2053. https://doi.org/10.1002/esp.2225.
Rouyet, L., Karjalainen, O., Niittynen, P., Aalto, J., Luoto, M., Lauknes, T.R., Larsen, Y., Hjort, J., 2021. Environmental controls of InSAR-based periglacial ground dynamics in a sub-arctic landscape. J. Geophys. Res. Earth Surf. 126, 1–24. https://doi.org/10.1029/2021JF006175.
Rouyet, L., Lauknes, T.R., Christiansen, H.H., Strand, S.M., Larsen, Y., 2019. Seasonal dynamics of a permafrost landscape, Adventdalen, Svalbard, investigated by InSAR. Remote Sens. Environ. 231, 111236 https://doi.org/10.1016/j.rse.2019.111236.
Van Everdingen, R.O., 2005. Multi-language glossary of permafrost and related ground-ice terms. In: Int. Permafr. Assoc. Terminol. Work. Gr.
Yang, W., Wang, Yujie, Wang, Yunqi, Ma, C., Ma, Y., 2020. Retrospective deformation of the Baige landslide using optical remote sensing images. Landslides 17, 659–668. https://doi.org/10.1007/s10346-019-01311-7.
Zhang, S., Jiang, Q., Shi, C., Xu, X., Gong, Y., Xi, J., Liu, W., Liu, B., 2021. Application of Sentinel-1 and-2 images in measuring the deformation of Kuh-E-Namak (Dashti) NamakierIran. Remote Sens. 13, 1–18. https://doi.org/10.3390/rs13040785.